PHYSICAL SCIENCES

Enhanced dual-mode imaging: Superior photoacoustic and ultrasound endoscopy in live pigs using a transparent ultrasound transducer

Jaewoo Kim[1,2]†, Dasom Heo[1]†, Seonghee Cho[1,2], Mingyu Ha[1], Jeongwoo Park[1,3], Joongho Ahn[1,2], Minsu Kim[1], Donggyu Kim[1], Da Hyun Jung[4], Hyung Ham Kim[1]*, Hee Man Kim[5]*, Chulhong Kim[1,2]*

Dual-mode photoacoustic/ultrasound endoscopy (ePAUS) is a promising tool for preclinical and clinical interventions. To be clinically useful, ePAUS must deliver high-performance ultrasound imaging comparable to commercial systems and maintain high photoacoustic imaging performance at long working distances. This requires a transducer with an intact physical aperture and coaxial alignment of acoustic and optical beams within the probe, a challenging integration task. We present a high-performance ePAUS probe with a miniaturized, optically transparent ultrasonic transducer (TUT) called ePAUS-TUT. The 1.8-mm-diameter probe, fitting into standard endoscopic channels, aligns acoustic and optical beams efficiently, achieving commercial-level ultrasound and high-resolution photoacoustic imaging over long distances. These imaging capabilities were validated through in vivo imaging of a rat's rectum and a pig's esophagus. The ePAUS-TUT system substantially enhances feasibility and potential for clinical applications.

INTRODUCTION

The photoacoustic imaging (PAI) is based on the photoacoustic (PA) effect, where light energy is converted into ultrasound (US) through the thermoelastic expansion of targets upon pulsed light irradiation. PA images of living subjects can provide morphological information (e.g., vasculatures, cell nuclei, lipid formations, and melanin distribution), multiparametric functional information [e.g., the metabolic rate of oxygen, the oxygen saturation of hemoglobin (SO_2), and blood flow], and molecular information (e.g., targeted contrast agents) (*1*–*18*). Most beneficially, PAI is seamlessly integrated into existing US imaging (USI) devices, such as breast and thyroid US, intravascular US (IVUS), and endoscopic US (EUS) (*19*–*23*).

EUS is one of the most widely used diagnostic modalities in gastroenterology (*24*), pulmonology (*25*), and urology (*26*), providing relatively deep structural information with high spatial resolution and safety. However, because it obtains contrast from acoustic properties, EUS still suffers from low imaging contrast for soft tissues and insufficient functional imaging capability (*27*). To overcome these limitations, PAI capability has been added to existing EUS systems. Combining endoscopic PA and US (ePAUS) imaging can provide not only functional information (e.g., SO_2) and molecular information (e.g., lymphatic vessel and node localization with contrast agents) like the aforementioned PA imaging but also complementary structural information (e.g., stratified tissue, internal organs, and blood vessels) (*22*). These rich data are enabled by simultaneously acquiring high-resolution optical contrast-based PA images while maintaining the existing USI capabilities.

For the ePAUS probe to be clinically useful, three factors are important. First, for compatibility with commercial endoscopic channels, the optical and acoustic components must be coordinated in a small probe (<2.5 mm in diameter, including the medical tubing) driven by a torque coil. Second, for imaging wide and hollow gastrointestinal (GI) structures such as the esophagus or stomach, the PAI working distance must be long. Since arbitrarily adjusting the distance between the probe and imaging target is difficult, it is important to be able to cover a wide imaging range with a long working distance. Third, to be clinically notable, the regular US images in the combined ePAUS must have commercial-grade quality. The US images provide structural information about the stratified GI tract tissues and serve as a valuable reference in interpreting the original tissue layers of the PA vascular signal. To date, the clinical spread of ePAUS has been substantially limited by its poor US image qualities. Further advances depend on the development of a clinically notable ePAUS with high-performance imaging capabilities in both modalities.

Figure S1 shows various strategies to overlap the optical and acoustic beams in endoscopic probes. The easiest way is to tilt one or both beams. Basij *et al.*, Li *et al.*, and Wang *et al.* (*28*–*34*) tilted the optical beam. Instead, Liu *et al.* (*35*) tilted the needle transducer, and Bai *et al.* (*36*) tilted the US transducer, which in turn tilted the acoustic beam. Further, Piao *et al.* and Cao *et al.* (*37*, *38*) tilted both beams to make an overlapping area. However, because tilting does not align the two beams coaxially, the signal-to-noise ratios (SNRs) are not optimized outside the overlap area. Two main approaches have been investigated to coaxially align both beams, either using a ring US transducer with a hole in the center (*22*, *39*–*48*) or using an opto-US beam combiner (*49*–*53*). Using the former method, the wide active area needed for high sensitivity makes it difficult to reduce the size of the ring transducer, a key limiting factor in making a small endoscopic probe. Further, the distant focal spot of the ring US transducer prevents the optical beam from being highly focused

[1]Department of Electrical Engineering, Convergence IT Engineering, Mechanical Engineering, and Medical Device Innovation Center, Pohang University of Science and Technology (POSTECH), Pohang 37673, Republic of Korea. [2]Opticho Inc., Pohang 37673 Republic of Korea. [3]Department of Biomedical Convergence Science and Technology, School of Convergence, Kyungpook National University, Daegu 41566, Republic of Korea. [4]Department of Gastroenterology, Internal Medicine, Severance Hospital, Yonsei University College of Medicine, Seoul 03722, Republic of Korea. [5]Cancer Prevention Center, Yonsei Cancer Center, Severance Hospital, Yonsei University College of Medicine, Seoul 03722, Republic of Korea.
*Corresponding author. Email: chulhong@postech.edu (C.K.); loverkorea2009@gmail.com (H.M.K.); david.kim@postech.ac.kr (H.H.K.)
†These authors contributed equally to this work.

onto a near spot, resulting in poor transverse resolution. In addition, the ring US transducer itself suffers from side lobe artifacts. In two related approaches, Lin *et al.* (*54*) drilled a hole in the center of the transducer and Kim *et al.* (*55*) applied dark-field acoustic detection (i.e., X-ducers), which mimic the ring-shaped US transducer by crossing the acoustic axes of the two transducers. However, these studies showed poor USI performance for the same reasons as ring US transducers. In the latter method, using an opto-US beam combiner, it is even more difficult to efficiently position the beam combiner in the small probe. Cao *et al.* (*21*) achieved coaxial alignment between the two beams by inserting a very small opto-US beam combiner into the probe, then demonstrated its performance by imaging a human coronary artery ex vivo. However, this method reduces the USI quality due to multiple acoustic reflections from different surfaces of the coupler and multiple transmissions through different acoustic media.

In other words, concurrently enhancing PA and USI capabilities is considered conflicting so far. High-performance PAI, characterized by a high SNR, high resolution, and long working distance, necessitates coaxial alignment of the acoustic and optical beams. However, achieving such coaxial alignment degrades USI performance (e.g., with a ring-shaped transducer, X-ducers, or a beam combiner). The challenge lies in accomplishing high-performance PAI and USI simultaneously within an ePAUS probe small enough to be used with commercial endoscopes.

In this study, all the aforementioned challenges of ePAUS were successfully overcome by applying a transparent US transducer (TUT). We developed the smallest TUT yet (1 mm × 1 mm × 0.47 mm) with a wide bandwidth (61% at 21 MHz center frequency). The miniaturized TUT enables an elegant integration of the acoustic and optical beams within a miniaturized probe, enhancing clinical applicability through excellent dual-modality imaging performance without compromising either USI or PAI performance. The improved structural imaging of the probe was demonstrated by inserting it into a commercial endoscopic channel and imaging a porcine esophagus in vivo. Simultaneously, high-performance PAI with a long working distance of 12 mm was implemented. This advance enabled the imaging of intrapapillary capillary loops (IPCLs) in a breathing pig's esophagus. In addition, this probe demonstrated a high-performance USI capability, comparable to that of commercial EUS, allowing it to differentiate a rat's rectal anatomy and all layers of a pig's GI tract in vivo.

RESULTS

TUT fabrication process and acoustic and optical properties

A TUT requires a highly transparent piezoelectric material with an acoustic impedance that appropriately matches the impedance of each layer. Lead magnesium niobate-lead titanate (PMN-PT), lithium niobate (LNO), and polyvinylidene fluoride (PVDF) are widely used transparent piezoelectric materials that satisfy this requirement. LNO has a high curie temperature ($T_c = 1150$°C), which provides stability in the fabrication process, and PVDF has a high piezoelectric voltage constant ($g_{33} \cong 200 \times 10^{-3}$ V·m/C), allowing signals to be received across a broad bandwidth. Despite these advantages, we selected PMN-PT because it has a higher dielectric constant ($\varepsilon_0 = 895$) and a lower longitudinal velocity ($v = 4600$ m/s) than LNO and has a higher electromechanical coupling coefficient ($k_t \cong 0.6$) and piezoelectric charge constant ($d_{33} = 1190$ pC/N) than PVDF, qualities making it suitable for miniaturization (text S1 and fig. S2). The fabrication process of the TUT is depicted in Fig. 1A. Initially, both sides of a PMN-PT plate were lapped and polished to a designed thickness, and ITO (indium-tin-oxide) and gold were sputtered onto both faces of the polished PMN-PT to serve as electrodes. A nonconductive epoxy was poured over the sputtered surface as a matching layer. Once the epoxy had cured, the entire laminate was lapped and polished, and the same procedure was repeated with urethane. On the other side of PMN-PT, a backing block was bonded, and the finished stack was diced to the designed size. Then a microcoaxial cable was connected to both sides, and lastly, the transducer was coated. Figure 1B shows the layer structure and a photograph of the fabricated TUT. The optical transparency of the TUT is demonstrated by the letter "E," clearly visible below the transducer. Detailed fabrication procedures are described in the Materials and Methods.

Figure 1C shows the simulated acoustic performance of the TUT. The transducer simulation setup and performance measurement methods are described in Materials and Methods. The TUT has a center frequency of 20.0 MHz and a −6 dB bandwidth of 64.64%. The electrical impedance at the designed center frequency is 89 ohms. As can be seen from the simulated acoustic intensity field, an intensity greater than −6 dB relative to the maximum value extends from 1.64 to 8.28 mm from the probe, and the intensity peak occurs at 3.2 mm. Figure 1D shows the experimental acoustic performance of the TUT, with a center frequency of 21.2 MHz, a bandwidth of 61.9%, and an electrical impedance of 45.8 ohms at the center frequency. The optical transmittance of the TUT shows a peak of 78.9% at 700 nm and 71.7% transmittance at 532 nm, the wavelength used for imaging. The matching layers and ITO, respectively, show 90 and 80% transmittance at 532 nm (Fig. 1E). For comparison, acoustic performance simulations were performed on LNO-based and PVDF-based TUTs (text S1 and fig. S2). If a TUT with the same center frequency (20 MHz) and aperture size (1 mm × 1 mm) were to be fabricated with LNO or PVDF, it would be difficult to match the impedance, as the impedance of LNO is 4.45 kilohms and that of PVDF is 10.3 kilohms. Therefore, PMN-PT was selected as the most suitable piezoelectric material for the miniaturized TUT. In conclusion, the developed miniaturized TUT is competitive not only with conventional opaque US transducers but also with previously developed TUTs (*56*). Text S2 and fig. S3 compare its performance with that of opaque ultrasonic transducers, while table S1 details comparable aspects of previously produced TUTs.

ePAUS-TUT system and probe and performance benchmarks

The structure of this system can best be described by following the optical beam path. As the drawing in Fig. 2A illustrates, a 532-nm laser beam for PA excitation is guided to a collimator (The system operation is described in detail in text S3 and fig. S4). Light is transmitted to the scanning system through a 50-μm core multimode fiber (MMF), passes through a torque coil, and enters the probe. The probe combines an acoustic module with an optical module that transmits light from the scanning system. The acoustic module combines a housing and a TUT. The housing is a short metal tube with an outer diameter of 1.8 mm and a rigid part's length of 12 mm, with a perforated window for the TUT. The acoustic module is finalized by attaching the TUT to the housing horizontally, so that the US emission plane of the transducer is perpendicular to the lumen to be imaged. The optical module has only three simple components: the

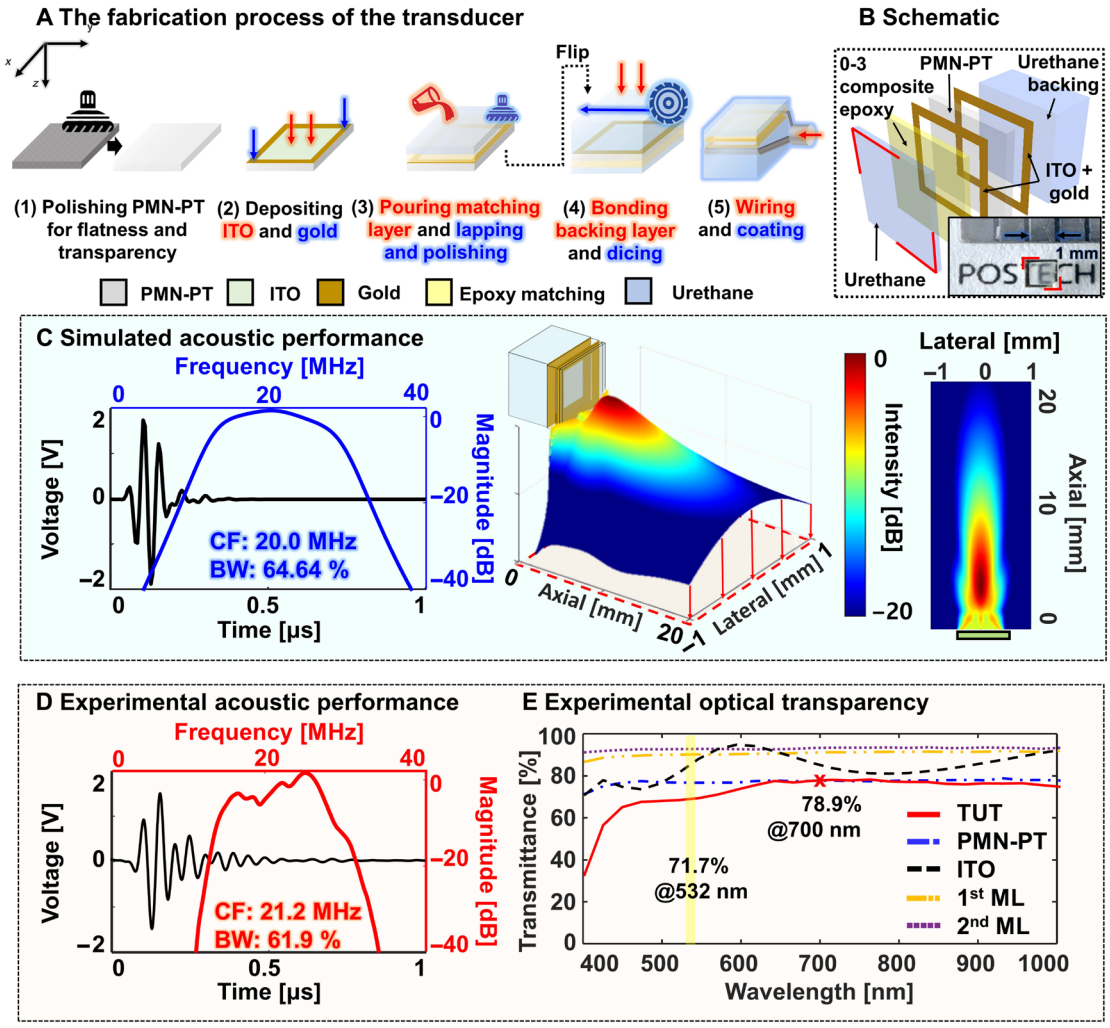

Fig. 1. Fabrication and operating characteristics of a TUT. (**A**) Fabrication of the TUT. (**B**) Schematic of the layer structure and (inset) photograph of the TUT. (**C**) Simulated and (**D**) Experimental acoustic performances. (**E**) Experimental optical transmittance. CF, center frequency; BW, bandwidth; and ML, matching layer.

MMF with a core diameter of 105 μm, a gradient index (GRIN) lens, and a right-angle prism. Light from the scanning system is directed onto the customized GRIN lens and reflected from a prism whose oblique surface is coated with aluminum. Afterward, the light passes through the TUT and makes a focus at a distance of 2 mm. The probe is then inserted into a medical tubing with an outside diameter of 2.45 mm. The lower right inset of Fig. 2A is a photograph of the ePAUS-TUT probe with the medical tubing. The system primarily operates in optical resolution mode, where the transverse resolution is determined by light. In contrast to existing optical resolution mode systems that achieve extremely high resolution by combining a single-mode fiber and a lens, this system uses an MMF and a lens, working in quasi-optical resolution mode, to provide a long working distance and enhance the transmission of light energy. Last, a coaxial structure within a 1.8-mm-diameter housing integrates the optics and the intact transducer without holes or a beam combiner. In this way, the acoustic and optical beams are combined on one axis without interfering with each other, enabling simultaneous acquisition of high-performance PAI and USI.

To evaluate the effect of the TUT on light scattering and absorption within the imaging probe, changes in the beam's shape and light intensity were monitored as it passed through each component (Fig. 2B). Panel #1 shows the light emerging from the prism without any obstruction, while panel #2 shows the beam's shape after passing through the TUT, and #3 shows the beam's shape after traversing both the TUT and the tube. In case of #1, the beam shape is close to the original beam shape from the MMF (750 μW). In #2, minor light scattering is observed, likely originating from the PMN-PT layer, yet it is evident that almost all modes maintain their original form (530 μW and 70% of the initial light). These results align with expectations, given that the simulated ideal TUT has a transparency of 71.7% at 532 nm. The beam shape in #3 exhibits minimal differences from that in #2 (502 μW), indicating a loss of 5% in the tube.

Figure 2C plots the spatial resolutions of captured PA and US images based on their distances from the probe. For resolution measurements, the referenced target-to-probe distance was calibrated using a circular pipe target (text S4). The measurements were conducted 15 times at a single point, and the graph displays the average value, along with error bars. The PA transverse resolution peaks at 91 μm at a distance of 2 mm, aligning with the focal length of the lens, and subsequently degrades as the light disperses. The PA axial resolution remains constant at approximately 70 μm after reaching

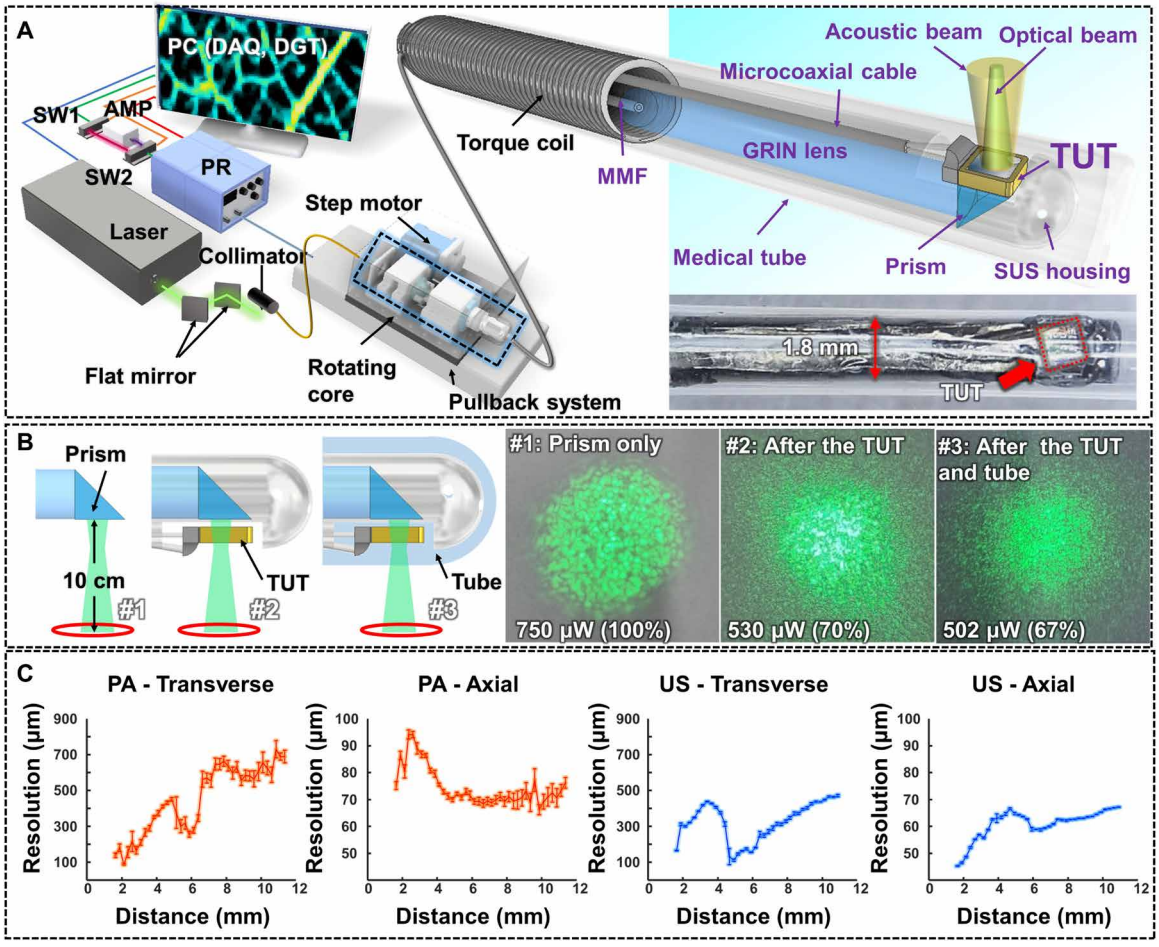

Fig. 2. System schematic and performance of the TUT-based ePAUS system. (**A**) Schematic of the overall ePAUS-TUT system and a photograph of the probe. (**B**) Optical beam shapes after each component: #1 immediately after the prism, #2 after passing the TUT, and #3 after passing through the TUT and tube. (**C**) PA and US transverse and axial resolutions as a function of distance. MMF, multimode fiber; SUS, steel use stainless; DAQ, data acquisition device; DGT, digitizer; PR, pulser/receiver; SW, switch; HSR, hollow-shaft slip ring; ORJ, optical rotary joint; and AMP, amplifier.

5 mm. The US transverse resolution exhibits its highest value of 110 μm at a distance of 5.4 mm, while the US axial resolution maintains a consistent measurement of about 62 μm from 5 mm onward. The PA signals measured at a distance of 11 mm demonstrate the long PAI working distance. Considering that the theoretical axial resolutions determined by the center frequency and bandwidth of the transducer are about 50 μm for US and 70 μm for PA (i.e., ~1.4 times higher than that of US), this result is consistent with the theoretical value (*57*). To validate the USI performance of ePAUS-TUT, comparative imaging tests were conducted using a conventional EUS, with the details described in text S5 and fig. S5. Furthermore, to demonstrate the PA and USI capabilities of ePAUS-TUT, in vitro imaging of a leaf skeleton was performed and presented in text S6 and fig. S6.

In vivo rectal imaging in a rat

To demonstrate the imaging capabilities of the ePAUS-TUT, PA and US images of the rectal wall were captured in vivo (Fig. 3). All PA/USI results were obtained with 6.2 mJ/cm^2 laser illumination, a 10 Hz B-scan rate, and a 0.25 mm/s pullback speed. The maximum SNRs of the rat rectal images are 38 dB for PA and 61 dB for US. Figure 3A shows three-dimensionally (3D) rendered overlaid PA/US, translucent PA/US, and depth-encoded PA-only images (movie S1). The inset photo shows the experimental concept. For more accurate anatomical analysis, the cross-sectional overlaid PA/US image slices indicated by blue squares (#1 to #3) in the 3D-rendered overlaid PA/US image in Fig. 3A are shown in Fig. 3B. In all three image slices, the PA signals are distributed along the rectal wall, originating from both small shallow blood vessels near the surface and large ones located more deeply. In the US images, strong US signals can be acquired even at the depths of over 12 mm. In panel #1, close to the anus, the dense pelvic floor muscle exhibits a strong US speckle pattern. The PA signals are distributed within 800 μm below the mucosal surface. The blue area represents the capillaries, and the yellow area represents the arteriolar and venular networks. In panel #2, hyperechoic areas such as the pubic bone are clearly distinguished. The symmetrical hyperechoic characteristic of the pubic bone is prominent and can be better observed in movie S2. In the movie, the initially separated pubic bone US signals on both sides merge into one as they approach the anus, and the bladder is visualized as a hypoechoic area between the pubic bones. The inset of panel #2 visualizes the layered structure of the PA signals and the

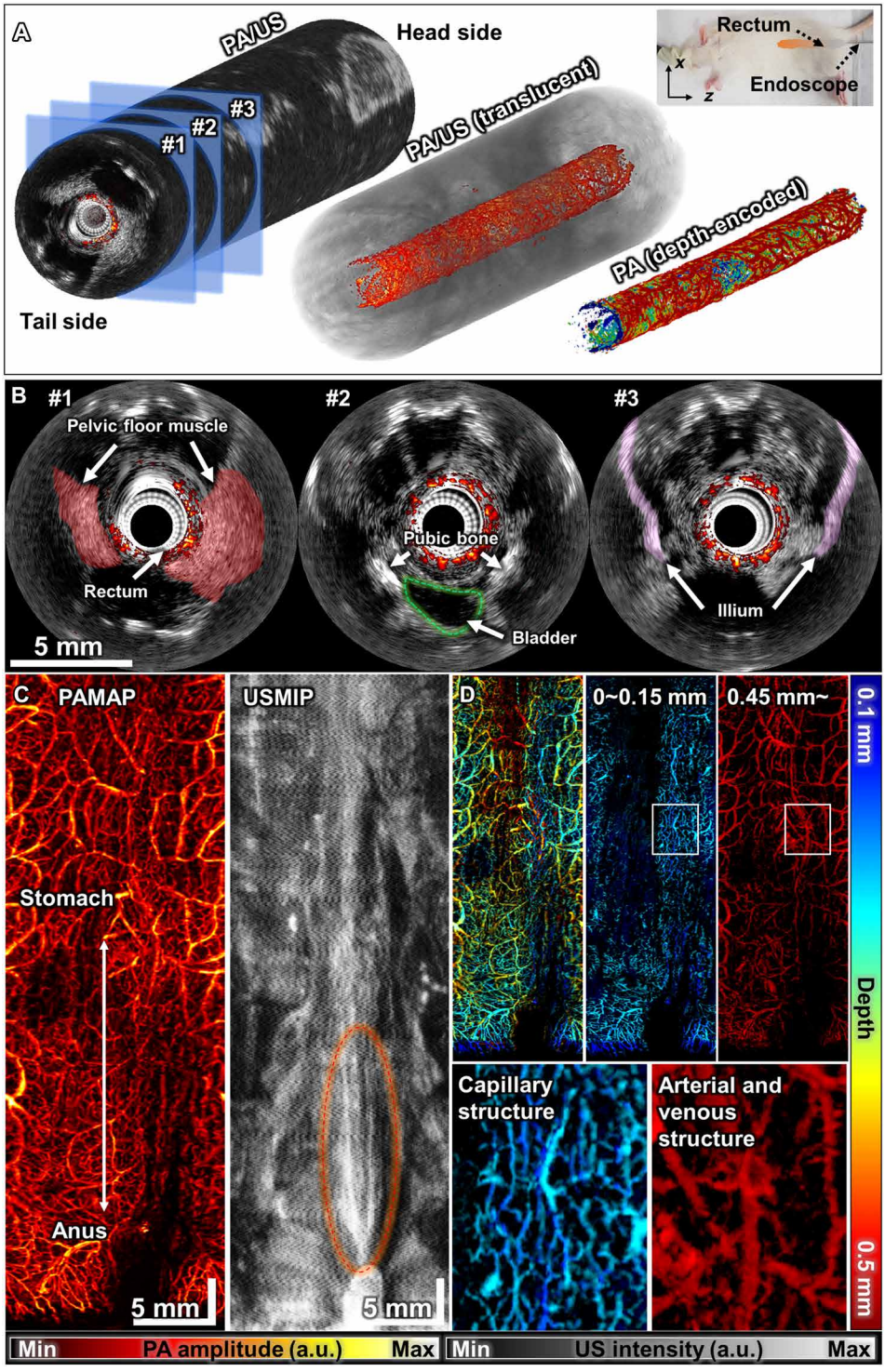

Fig. 3. Endoscopic PA/USI of a rat's rectum in vivo. (**A**) 3D-rendered overlaid PA/US, translucent PA/US, and depth-encoded PA-only images (movie S1). (**B**) Cross-sectional overlaid B-mode PA/US images indicated by numbers in (A). (**C**) PA MAP and US MIP images. (**D**) Three depth-encoded PA MAP images: The entire depth, from 0- to 0.15-mm deep, and below 0.45 mm. Insets are magnified images from the boxes in (D). All scale bars, 5 mm.

depth-dependent differences in vessel diameters. The capillaries are abundant in the deep lamina propria, while the arteries and veins are primarily located in the adjacent submucosa layer.

The present experimental results are consistent with the findings of previous studies (*58*, *59*). In panel #3, the symmetrical ilium structure centered around the rectum can be identified, demonstrating that the rat's body anatomy can be distinguished at a high level with the improved US quality. Figure 3C shows PA maximum amplitude projection (PA MAP) and US maximum intensity projection (US MIP) images transformed into a Cartesian coordinate system. In the PA MAP image, the vascular network of the rectal wall is clearly visualized. In the US MIP image, highly echoic materials such as bone appear with a high intensity, and the pubic bone is seen as two separate hyperechoic lines, indicated by the red dashed elliptical circle. These US signals from the pubic bones are merged into one as they approach the anus, which is consistent with the bone anatomy of the rat. Figure 3D shows three depth-encoded PA MAP images: the entire depth, from 0 to 0.15 mm, and below 0.45 mm. The depth-encoded PA MAP image covering 150 μm below the surface shows the epithelial vascular network, with densely distributed small diameter vessels. The magnified inset confirms the capillaries in the epithelial layer. In contrast, the depth-encoded PA MAP image of depths over 450 μm shows less densely distributed large vessels. The magnified inset identifies the arterial and venous networks in the mucosal layer. Judging from the quality of all these images, PA/USI is expected to contribute to the analysis of the rectal vascular structure and provide overall anatomical observations in monitoring lesions such as those caused by GI diseases.

In vivo esophageal imaging in a pig

To demonstrate the clinical potential of the ePAUS-TUTs system, preclinical imaging was performed on a pig's esophagus (Fig. 4, fig. S7, and movie S3). The experimental environment was designed to mimic practical clinical scenarios. The pig was fasted for 1 day, and before imaging, the stomach and esophagus were filled with water. All imaging parameters, such as the laser power, the B-scan rate, and the pullback speed, were maintained identical to those in the previously described rat imaging. The maximal SNRs of the pig's esophagus images were 40 and 59 dB for PAI and USI, respectively. Specific details are provided in Methods and Materials. The ePAUS-TUT probe, protected by a medical tubing with a diameter of 2.45 mm, was smoothly inserted into a commercial endoscope (GIF Q260J, Olympus Corporation, Japan) through a 3.2-mm-diameter imaging channel (Fig. 4A). Figure 4B shows a 3D-rendered overlaid PA/US image of the pig's esophagus, with a total length of 6 mm. The red and green boxes represent the cross-sectional vertical and radial views, respectively. Figure 4C shows the vertical view image designated by the red box in Fig. 4B. The cross-sectional US image in the vertical view clearly defines the leiomyoma structure along the *z*-axis direction and its distribution inside the adventitia. The layered structure is clearly visualized in the magnified image of the red box in Fig. 4C. This magnified image distinctly delineates all nine layers constituting the esophageal wall (table S2). The PA signals well visualized the distribution of IPCLs along the epithelial surface near the probe. For a more detailed examination, Fig. 4D (#1 to #3) shows the cross-sectional overlaid PA/US images in the radial views outlined with green boxes in Fig. 4B. In radial-view #1, six layers from the first epithelium to the muscularis propria are acoustically visualized over an imaging depth of 12 mm. Note that the echogenicity of each layer forming the esophageal wall is described in text S7 and table S2. The green box in radial-view #1 is magnified to provide detailed information about the stratified layer structure. Epithelial layers 1 and 2, the closet layers to the inner lining of the esophagus, can be observed, with hyperechoic and hypoechoic layers arranged sequentially. The lamina propria is hyperechoically delineated. Note that that the echogenicity of the lamina propria differs depending on the center frequency of the transducer. At frequencies below 20 MHz, it is generally observed as hypoechoic. However, at a frequency above 20 MHz, it appears as hyperechoic, as in our case (*60*). Next, the muscularis mucosae, which is the boundary between the mucosa and submucosa, is indicated as a thin hypoechoic layer. Following this, the submucosa and muscularis propria are distinguished by their hyperechoic and hypoechoic characteristics. Furthermore, by leveraging the layer structures from the US images, we could trace the blood vessel layers in the PA image. This capability allowed us to confirm the visualization of the IPCLs in the epithelial layer and the mucosal vessels in the lamina propria layer. The cross-sectional US image in the radial-view #2 shows the three layers constituting the muscularis propria. These layers are more clearly observed in the magnified image. The first and third hypoechoic layers originate in the inner circular muscle and outer longitudinal muscle, respectively, while the thin hyperechoic layer in between originates in the connective tissue. Last, the hyperechoic layer outside the muscularis propria corresponds to the adventitia. The cross-sectional overlaid PA/US image in radial-view #3 confirms the long working distance of the ePAUS-TUT system, achieved by acquiring the PA signal at a distance of 10.3 mm from the center. A leiomyoma structure is ultrasonically observed between the adventitia and muscularis propria. It is well-known that the echogenic characteristics and location of the hypoechoic region make it easy to identify a tumor (*61*). The magnified image shows blood vessels at a depth of 200 μm from the mucosal surface, which correspond to the IPCLs within the epithelial layer. Figure 4E, a PA MAP image, shows the vasculature of the pig's esophagus. Small diameter submucosal blood vessels are visualized, and IPCLs are marked by discrete strong signals. In conclusion, through this experiment, the nine-layer structure of the esophageal wall is clearly visualized from the US images, and the distribution of IPCLs in the mucosal layer is observed in the PA images. The ePAUS-TUT simultaneously provides high-quality acoustic anatomical images and optical vasculature images. Notably, conducting this experiment in conditions similar to an actual clinical environment goes far to confirm the clinical applicability of the ePAUS-TUT system.

DISCUSSION

The ePAUS, a clinically promising application of PAI, offers the benefits of functional PA imaging in addition to providing structural information from EUS imaging. To facilitate the easy application of ePAUS in the GI clinical setting, several conditions must be satisfied. The probe, including medical tubing, must have a diameter of 2.5 mm or less, and it should be flexible enough to be inserted into a commercial endoscope's channel. After these essential criteria are satisfied, both the PA and USI must perform at a high level. Here, coaxial alignment between the acoustic and optical beams is crucial for achieving long working distances, high SNRs, and the uniform illumination necessary for PA imaging. Historically, however, this coaxial alignment has often led to poor USI performance, as seen with ring-shaped transducers, hollow transducers, X-ducers, and beam combiners. In conclusion, although simultaneously achieving high performance in PAI and USI has been considered a daunting task, this study demonstrates that the ePAUS-TUT system successfully meets all these challenges.

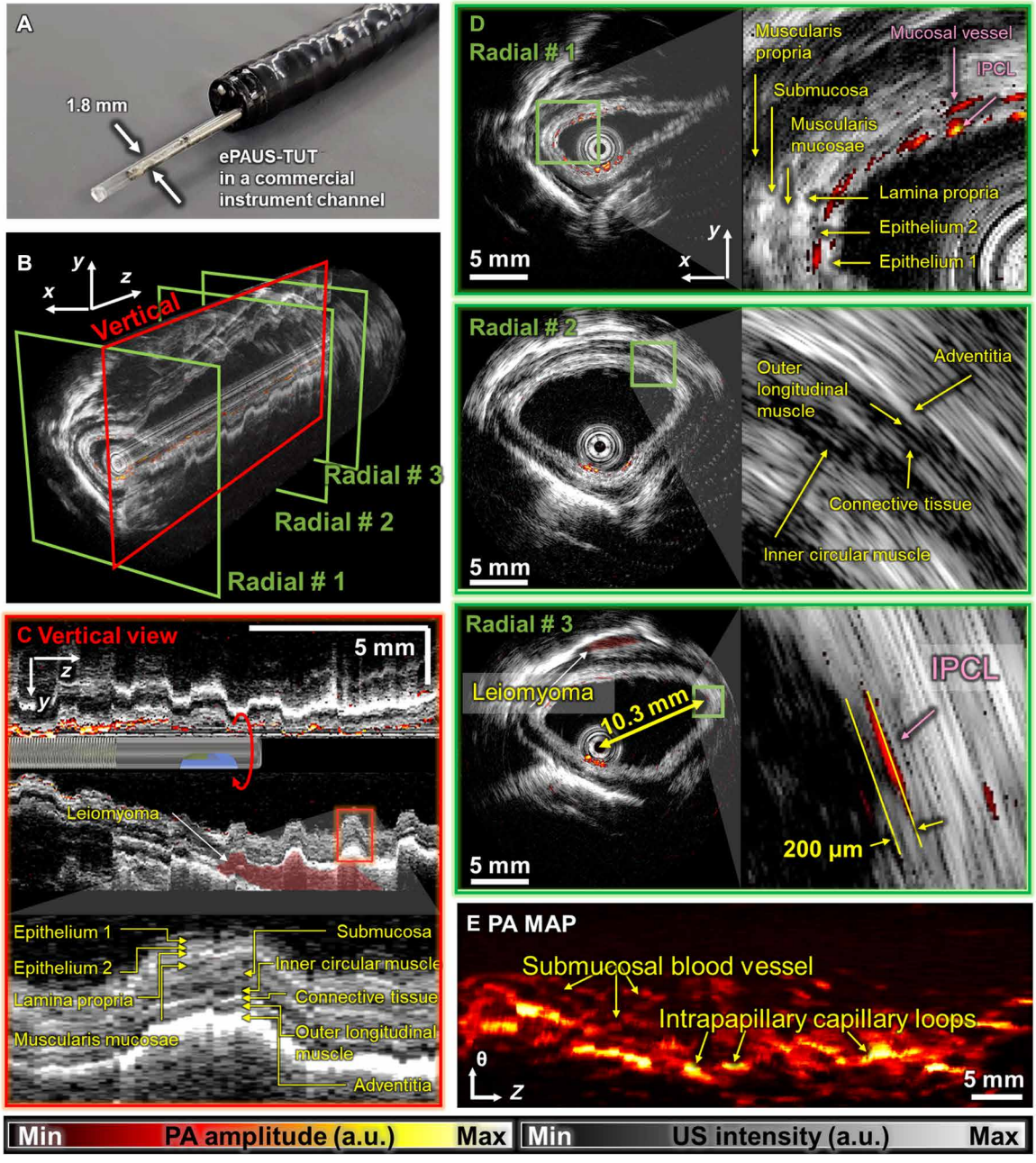

Fig. 4. Endoscopic PA/USI of a pig's esophagus in vivo. (**A**) Photograph of the ePAUS probe inserted into a commercial endoscope. (**B**) 3D-rendered overlaid PA/US image of a pig's esophagus. (**C**) Cross-sectional PA/US image cut along the vertical direction in (B). (**D**) Cross-sectional PA/US images (#1 to #3) cut along the radial direction in (B). (**E**) PA MAP image of the pig's esophagus. IPCL, intrapapillary capillary loops. All scale bars, 5 mm.

We successfully overcame the poor USI performance of previously developed ePAUS systems (*22*, *49*, *54*, *55*) by using a TUT. The developed ePAUS-TUT satisfies all the previously mentioned conditions for clinical applications. By incorporating an ultrasmall TUT (1×1 mm^2) into the ePAUS, the probe diameter can be reduced to as low as 1.8 mm, comfortably below the standard endoscopic channel diameter of 2.45 mm. By placing the TUT in the optical path, we achieved straightforward and compact coaxial alignment between the acoustic and optical beams. The coaxial arrangement maintains the transducer's central aperture, avoiding the side-lobe issues seen with ring-shaped transducers or hollow transducers. In addition, without a beam combiner, multiple US reflections are avoided, enhancing the USI performance. Moreover, the coaxial structure provides a long optical-acoustic overlap area, ensuring high SNRs, uniform illumination, and a long working distance in PA imaging.

Compared to the previous ePAUS system, the ePAUS-TUT offers several practical advantages from a clinical perspective. The first advantage is enhanced clinical applicability through structural improvements. In previous studies (*41*, *62*, *63*), the use of high laser pulse energy and/or complex optical structures required rigid probe bodies with large

diameters. However, the ePAUS-TUT achieves a high PA imaging SNR through its coaxial structure, enabling miniaturization and flexible driving via a torque coil. The flexible probe can be inserted into conventional endoscopes, expanding its imaging capabilities to areas inaccessible by rigid endoscopes, such as the esophagus and stomach. Further, the thin diameter, less than 2.5 mm, fits perfectly in standard endoscope channels. The clinical potential is successfully demonstrated here via in vivo porcine esophageal imaging, simulating clinical processes. In addition to its structural improvements, the second clinical advantage of ePAUS-TUT lies in its high-performance USI capability, comparable to that of commercial EUS, and its high-performance PAI with a long working distance. Because conventional EUS is used to effectively distinguish the layers in the GI tract and diagnose tumor, the reduced USI capabilities achieved in previous ePAUS studies (*22*, *49*, *54*, *55*) made those system unsuitable for clinical translation. Our ePAUS-TUT successfully provides US images of similar quality to those from commercial EUS. In addition, the importance of a long working distance in endoscopic PAI has been repeatedly mentioned (*54*, *64*), and the long PAI working distance (beyond 10 mm) of the ePAUS-TUT is very helpful for imaging the irregular surface of the GI tract. As a result, our system demonstrated a notable improvement in key imaging performance metrics (e.g., imaging range versus resolution for PAI and USI, compared to the previous ePAUS systems (*22*, *55*) (see table S3).

This study has experimental limitations, and there is potential for further development of the probe. First, the piezoelectric material may deteriorate in the manufacturing process. When artificially lapping and polishing to achieve the desired thickness, depolarization may occur, potentially destroying the domain structure of the piezoelectric material. In addition, stress applied to the piezoelectric plate during dicing may weaken its piezoelectric properties. Repolarizing the transducer can be one way to improve the piezoelectric performance. Repolarization helps realign the domains and relieves internal stress, thereby improving the overall performance of the piezoelectric material. Second, the PA SNR can be improved by increasing the transparency of the TUT. The optical damage threshold of the TUT limits both the laser pulse energy and repetition frequency, which directly affect the imaging depth and speed, respectively. For miniaturization, the piezoelectric material of the TUT was limited to using PMN-PT. However, the complex perovskite structure of PMN-PT causes more light scattering than low-crystalline PVDF or LNO, which have simpler crystal structures. Moreover, the complex ferroelectric domain structure of PMN-PT scatters light at domain boundaries. While other matching materials have high transparency (approximately 80 to 90%), PMN-PT has a transparency of approximately 70 to 80% at best, for the reasons mentioned. The more layers there are, the lower the total light transmittance. Scattering can be reduced by reducing the number of domain walls through AC poling, thereby improving transparency of the PMN-PT (*65*–*67*).

Furthermore, achieving a uniform coating layer over the entire transducer is crucial for maintaining transparency. An uneven coating can result in light scattering and consequent loss of optical transparency, making the TUT easily damaged by the laser or distorting the laser path. To address this issue, the appropriate vacuum conditions and the correct temperature during parylene coating deposition must be explored.

As a follow-up to this study, several clinical applications can be suggested. First, by applying an acoustically couplable gel or water-filled balloon structure to this endoscope, it could be used in pulmonology to diagnose lung tumors (*32*), or to study chronic obstructive pulmonary disease by observing airway wall thicknesses and vessel structures (*68*). Second, in urology, since the majority of bladder cancers are superficial (*69*), this endoscope could be used to diagnose the depth of tumor invasion and assess malignancy. Third, the most promising application is in cardiology. IVUS is currently one of the most widely used diagnostic methods in cardiology, but it faces problems such as low lateral resolution and lack of functional information. Therefore, many studies are underway to integrate optical imaging functions such as optical coherence tomography (OCT), near-infrared spectroscopy (NIRS), and PAI. One of the biggest obstacles in manufacturing an IVUS probe that simultaneously captures US and optical images is the limited space inside the probe. IVUS probes should be thinner than endoscopic probes, and the importance of efficient space utilization becomes more pronounced in miniaturized probes. By reducing the size of the probe to less than 1 mm and switching to a wavelength of 1720 nm, which has high absorption for lipids, the size and shape of a lipid core can be determined using PA imaging. Alternatively, space-saving TUT-based integration with other optical imaging devices such as OCT can be used to detect thin-cap fibroatheroma. This information can be used to analyze the rupture vulnerability (*70*).

In addition, other future work can be suggested. The first is an in vivo functional PA imaging (e.g., SO_2) study using multiple optical wavelengths (*71*, *72*). Further, molecular PA/USI using exogenous contrast agents can be implemented. To prove the concept, we performed endoscopic PA/USI with indocyanine green, a U.S. Food and Drug Administration–approved contrast agent, in phantoms (text S8 and fig. S8). Alternatively, deeper PA imaging may be possible by using the NIR wavelengths, where blood absorption and tissue scattering are relatively low (*16*, *72*–*75*).

Second is a front-viewing ePAUS. For some clinical uses, the scanning may need to be changed from side viewing to forward viewing, depending on the shape of the target (e.g., when imaging a target that is planar rather than tubular). Conventional opaque transducers make it difficult to overlap the areas of the acoustic and optical beams for forward-viewing endoscopes. However, TUT-based forward-viewing endoscopes could accomplish coaxial alignment by using optical scanners, such as fiber scanners.

Third, the most promising future development of the TUT endoscope project could be integrating it with other optical modalities, such as white light endoscopy, fluorescence (FL), OCT, and NIRS. The TUT makes it such optical integration structurally easy. To demonstrate this proof of concept, we integrated our system with a FL imaging setup and conducted experiments in a phantom (see text S8 and fig. S8). On the basis of these promising results, we anticipate that this multimodal approach can be extended to in vivo applications in the future.

In summary, we began by successfully developing a PMN-PT–based ultrasmall TUT. Subsequently, we applied it to ePAUS, achieving structural and performance improvements and creating a probe optimized for clinical use. The ePAUS-TUT exhibits high-performance USI, comparable to that of commercial products, and high-performance PAI with a high resolution, high SNR, and a long working distance of over 10 mm. The ePAUS-TUT is easily inserted into a commercial endoscope channel, as demonstrated here by in vivo imaging of a pig's esophagus. The system could differentiate the layers in the GI tract, diagnose a leiomyoma, and visualize vascular distribution. This study has convincingly demonstrated an increase in the clinical applicability of ePAUS, paving the way for anticipated future applied research.

MATERIALS AND METHODS

KLM modeling

The transducer's design is based on Krimholtz-Leedom-Matthaei modeling, an equivalent circuit modeling method (*76*). We used PiezoCAD transducer simulation software (Sonic Concepts Inc.) with a library of various material data, such as the longitudinal velocity, dielectric constant, coupling coefficient, and attenuation. In TUT design, each layer requires high transparency and an acoustic impedance that matches well with the other layers, so selecting the material for each layer is an important step. Commonly used transparent piezoelectric materials satisfying these criteria include PMN-PT, LNO, and PVDF. We selected PMN-PT because it has a higher dielectric constant ($\varepsilon_0 = 895$) and a lower longitudinal velocity ($v = 4600$ m/s) than LNO and has a higher electromechanical coupling coefficient ($k_t \cong 0.6$) and piezoelectric charge constant ($d_{33} = 1190$ pC/N) than PVDF, qualities making it suitable for miniaturization (text S1 and fig. S2). As a result, the TUT was designed with PMN-PT as the piezoelectric material, 0-3 ceramic composite epoxy as the first matching layer and urethane as both the second matching layer and the backing layer. The thickness of the piezoelectric material was determined by the half wavelength of the TUT's center frequency, and the thickness of the matching layer was determined by its quarter wavelength. Through iterative simulations and adjusting of parameters, an optimized design was established. The TUT's final aperture measured 1 mm × 1 mm along the *x* and *y* axes, respectively. The TUT consisted of four layers: urethane, 0-3 ceramic composite epoxy, PMN-PT, and urethane. The four layers had thicknesses of 28, 46, 90, and 300 μm, respectively.

TUT fabrication

Both faces of the PMN-PT plate (PMN-28%PT, CTS Corp.) were lapped with calcined aluminum oxide powder (3 μm, Logitech Ltd.) and polished with colloid (SF1 polishing suspension, Logitech Ltd.) to a thickness of 90 μm, and a 250-nm-thick layer of ITO was sputtered as an electrode on the polished side. Along the edges chrome and gold were sputtered to 500 and 1000 Å thicknesses, respectively. The first matching layer, nonconductive epoxy, was poured onto one side of the PMN-PT plate and cured. The first matching layer was a mixture of epoxy (EPOTEK 301, Epoxy Technology Inc.) and ceramic particles (silicon dioxide, Sigma-Aldrich). The cured epoxy was lapped to a thickness of 46 μm. Urethane (Crystal Clear 202, Smooth-on), the second matching layer, was poured on top of the already processed first matching layer, and the same process was repeated to adjust the thickness to 28 μm. The entire laminate stack was diced to 1 mm × 1 mm along the *x* and *y* axes. After the stack was diced, a urethane block was attached with urethane to the PMN-PT surface opposite the matching layer. A 38 AWG micro-coaxial cable (9438 WH033, Alpha Wire) was connected to both sides of the PMN-PT with conductive epoxy (H20E, Epoxy Technology Inc.). Afterward, for reliable insulation, a 1-μm-thick urethane and parylene were coated on each surface of the transducer as the final step of fabrication.

Acoustic property measurement

The pulse-echo signal was measured using a pulser/receiver (5073PR, Olympus) under the conditions of 0 dB gain, 2 μJ energy per pulse, 50 ohms damping, and a 200 Hz pulse repetition rate. The signal reflected from the target was analyzed with a fast Fourier transform. For endoscopic transducers, it is difficult to measure the impedance of the transducer itself because the impedance of a long coaxial cable affects the overall impedance during the measurement. To reduce the effect of the cable, the wire was shortened to 5 cm, and the impedance of the transducer was measured in water with an impedance analyzer (E4990A, Keysight).

Optical property measurement

The optical transmittance was separately measured for the individual urethane layers, the 0-3 ceramic composite epoxy layer, the ITO layer, and the PMN-PT layer, as well as for the final TUT incorporating all the layers. The measurements were conducted at wavelengths of 400 to 1000 nm, using a ultraviolet-visible spectrophotometer (S-3100, SCINCO CO. LTD). To measure the transmittance of each layer, a specimen for measurement was prepared with a size of 10 mm × 10 mm. The configuration and thickness, except for the size, were the same as the actual transducer.

ePAUS-TUT system.

Figure 2A is a schematic diagram of the ePAUS-TUT system. The pulsed Nd:yttrium-aluminum-garnet laser (AWAVE-532-1W-10K, Advanced Optowave), with a 10 ns pulse width and a 532 nm wavelength, generates the PA signal. A pair of adjustable flat mirrors aligns the laser beam with the collimator (F230FC-A, Thorlabs). The light is then coupled to a laboratory-made optical rotary joint (ORJ) via a 50-μm core MMF (M42L05, Thorlabs). The pulser/receiver (5073PR, Olympus) performs US transmission/reception and PA signal reception. The preamplifier (ZFL-500LN+, Mini-Circuits) is applied to only the PA signal, amplifying it by about 25 dB. Where the PA and US signals share the same signal line, to select the amplifier path for PA signal acquisition only, a data acquisition device (PCie6321, National Instruments) controls two digital switches (ZX80-DR230-S+, Mini Circuit). Both PA and US signals are alternately acquired by a digitizer (ATS9350, AlazaTech) at a sampling rate of 250 MS/s. The scanning system's step motor (EDCI60V24, Erae Tech) provides torque for rotation, and the motorized linear stage (LTS150, Thorlabs) enables pullback translation in the elevational direction. A hollow shaft electrical slip ring (SNG-012, SENRING) transmits the signal from the rotating endoscope to the stationary pulser/receiver. We fabricated the ORJ by coaxially coupling two collimators (PAF2-A4A, Thorlabs) to achieve a highly durable joint that would not be damaged at high laser peak powers. For the in vivo imaging experiments, B-scan images were acquired at 10 fps and a pullback rate of 0.25 mm/s.

Endoscopic probe fabrication

The probe is composed of an acoustic module and an optical module. The acoustic module was manufactured by aligning the TUT and attaching it to the housing tube, a stainless-steel pipe with a custom-fabricated window on one side, an outer diameter of 1.8 mm, an inner diameter of 1.66 mm, and a length of 12 mm. The TUT was attached to the housing tube so that the axes of the acoustic beam and the rotation were perpendicular to each other. The optical module consists of three simple components: an MMF optical fiber with a 105-μm core, a GRIN lens, and a prism. After the excitation light passes through the MMF (M43L05, Thorlabs), it is directed to the custom GRIN lens (customized GRIN lens, GRINTECH GmbH). The GRIN lens makes a focal point 2 mm away from the TUT surface in a water environment. The optical beam is reflected from the prism (customized prism, GRINTECH GmbH) and passes

through the TUT. Last, the probe and torque coil were encapsulated in a water-filled Pebax tube with an outside diameter of 2.45 mm.

Resolution measurements

The axial and transverse resolutions were measured using a surgical blade. The surgical blade was fixed on a three-axis stage parallel to the axis of rotation of the probe and was imaged radially away from the probe over a distance range of 1.65 to 11.4 mm at 0.25-mm intervals. The surgical blade was imaged by rotating the probe as in a real imaging environment. From the B-scan image of the surgical blade, line profiles were extracted in the transverse and axial directions, then the transverse resolution was fitted to the cumulative distribution function of the Gaussian function, and the axial resolution was fitted to the Gaussian function. The transverse resolution was derived by extracting the derivative of the fitted graph, i.e., the full width at half-maximum (FWHM) of the Gaussian function, then dividing the FWHM in "pixels" by the "number of A-lines per B-scan" and multiplying by the circumference, defined as a circle whose radius is the distance between the center and the target. The axial resolution was calculated as the FWHM of the axial line profile. All data were measured 15 times at each location, and the mean and SD were calculated.

Rat's rectum imaging in vivo

The rat imaging experiments were performed according to the laboratory animal protocol approved by the Institutional Animal Care and Use Committee of Pohang University of Science and Technology (POSTECH-2024-0025). A 15-week-old Sprague Dawley rat's rectum was imaged in vivo. Before the experiment, the animal was fasted for 24 hours to empty its rectum. Before imaging, the animal was initially anesthetized with 4% isoflurane vaporized by inhalation gas (1.0 liter/min flow rate) and then kept under anesthesia with 1.5% isoflurane during the imaging. For acoustic coupling, the rectum was filled with water with a syringe. During the experiment, the animal was kept warm with an infrared lamp. After closing one end of the medical tubing with adhesive and filling it with water, the imaging probe was inserted. Then, the entire tube-probe structure was inserted into the imaging area to perform rotational imaging. The wavelength of the laser for PA excitation was 532 nm, and the optical power emitted from the probe's distal end was 6.2 mJ/cm^2, lower than the American National Standards Institute (ANSI) limit for the skin surface. The total imaged length of the rectum was 70 mm. The pullback was performed at a rate of 0.25 mm/s, taking approximately 4.6 min to obtain an entire single volume of data.

Pig's esophagus imaging in vivo

The pig imaging experiments were conducted by a company providing nonclinical services and were performed by gastroenterologists. The pig experiments were performed in accordance with the company's ethical guidelines for animal research. A 16-week-old laboratory pig (YLxDD) was used for in vivo imaging. The animal was fasted for 24 hours to empty the stomach and esophagus. An Olympus GIF Q260J was used for endoscopic procedures. To achieve acoustic coupling between the endoscope and tissue, the pig's esophagus was filled with water through the instrument channel after endoscope insertion. The ePAUS-TUT probe, protected by a 2.4 m length of medical tubing, was then inserted into the endoscopic channel. The laser wavelength for PA excitation was 532 nm, and the light power emitted from the distal end of the probe was measured to be 6.2 mJ/cm^2, confirming it to be below the ANSI limits for skin surface exposure. Pullback scanning was performed automatically, using a motorized stage. The total pullback length of the imaged esophagus was 70 mm, and the pullback was performed at 0.25 mm/s, taking approximately 4.6 min to capture data for an entire single volume.

Supplementary Materials

The PDF file includes:

Supplementary Text S1 to S8
Figs. S1 to S8
Tables S1 to S3
Legends for movies S1 to S3

Other Supplementary Material for this manuscript includes the following:

Movies S1 to S3

REFERENCES AND NOTES

1. J. Weber, P. C. Beard, S. E. Bohndiek, Contrast agents for molecular photoacoustic imaging. *Nat. Methods* **13**, 639–650 (2016).
2. J. Kim, J. Y. Kim, S. Jeon, J. W. Baik, S. H. Cho, C. Kim, Super-resolution localization photoacoustic microscopy using intrinsic red blood cells as contrast absorbers. *Light Sci. Appl.* **8**, 103 (2019).
3. J. W. Baik, H. Kim, M. Son, J. Choi, K. G. Kim, J. H. Baek, Y. H. Park, J. An, H. Y. Choi, S. Y. Ryu, Intraoperative label-free photoacoustic histopathology of clinical specimens. *Laser Photon. Rev.* **15**, 2100124 (2021).
4. J. Kim, B. Park, J. Ha, I. Steinberg, S. M. Hooper, C. Jeong, E.-Y. Park, W. Choi, T. Liang, J. S. Bae, Multiparametric photoacoustic analysis of human thyroid cancers in vivo. *Cancer Res.* **81**, 4849–4860 (2021).
5. J. Kim, G. Kim, L. Li, P. Zhang, J. Y. Kim, Y. Kim, H. H. Kim, L. V. Wang, S. Lee, C. Kim, Deep learning acceleration of multiscale superresolution localization photoacoustic imaging. *Light Sci. Appl.* **11**, 131 (2022).
6. T. T. Wong, R. Zhang, C. Zhang, H.-C. Hsu, K. I. Maslov, L. Wang, J. Shi, R. Chen, K. K. Shung, Q. Zhou, Label-free automated three-dimensional imaging of whole organs by microtomy-assisted photoacoustic microscopy. *Nat. Commun.* **8**, 1386 (2017).
7. M. Lakshman, A. Needles, Screening and quantification of the tumor microenvironment with micro-ultrasound and photoacoustic imaging. *Nat. Methods* **12**, iii–v (2015).
8. M. A. Pleitez, A. A. Khan, A. Soldà, A. Chmyrov, J. Reber, F. Gasparin, M. R. Seeger, B. Schätz, S. Herzig, M. Scheideler, Label-free metabolic imaging by mid-infrared optoacoustic microscopy in living cells. *Nat. Biotechnol.* **38**, 293–296 (2020).
9. I. Weidenfeld, C. Zakian, P. Duewell, A. Chmyrov, U. Klemm, J. Aguirre, V. Ntziachristos, A. C. Stiel, Homogentisic acid-derived pigment as a biocompatible label for optoacoustic imaging of macrophages. *Nat. Commun.* **10**, 5056 (2019).
10. J. Li, A. Chekkoury, J. Prakash, S. Glasl, P. Vetschera, B. Koberstein-Schwarz, I. Olefir, V. Gujrati, M. Omar, V. Ntziachristos, Spatial heterogeneity of oxygenation and haemodynamics in breast cancer resolved in vivo by conical multispectral optoacoustic mesoscopy. *Light Sci. Appl.* **9**, 57 (2020).
11. K. Basak, X. Luís Deán-Ben, S. Gottschalk, M. Reiss, D. Razansky, Non-invasive determination of murine placental and foetal functional parameters with multispectral optoacoustic tomography. *Light Sci. Appl.* **8**, 71 (2019).
12. S. Gottschalk, O. Degtyaruk, B. Mc Larney, J. Rebling, M. A. Hutter, X. L. Deán-Ben, S. Shoham, D. Razansky, Rapid volumetric optoacoustic imaging of neural dynamics across the mouse brain. *Nat. Biomed. Eng.* **3**, 392–401 (2019).
13. J. Rebling, M. Ben-Yehuda Greenwald, M. Wietecha, S. Werner, D. Razansky, Long-term imaging of wound angiogenesis with large scale optoacoustic microscopy. *Adv. Sci.* **8**, 2004226 (2021).
14. L. Li, D. Patil, G. Petruncio, K. K. Harnden, J. V. Somasekharan, M. Paige, L. V. Wang, C. Salvador-Morales, Integration of multitargeted polymer-based contrast agents with photoacoustic computed tomography: An imaging technique to visualize breast cancer intratumor heterogeneity. *ACS Nano* **15**, 2413–2427 (2021).
15. P. Zhang, L. Li, L. Lin, J. Shi, L. V. Wang, In vivo superresolution photoacoustic computed tomography by localization of single dyed droplets. *Light Sci. Appl.* **8**, 1038 (2019).
16. L. Li, A. A. Shemetov, M. Baloban, P. Hu, L. Zhu, D. M. Shcherbakova, R. Zhang, J. Shi, J. Yao, L. V. Wang, Small near-infrared photochromic protein for photoacoustic multi-contrast imaging and detection of protein interactions in vivo. *Nat. Commun.* **9**, 2734 (2018).
17. J. Weber, L. Bollepalli, A. M. Belenguer, M. Di Antonio, N. De Mitri, J. Joseph, S. Balasubramanian, C. A. Hunter, S. E. Bohndiek, An activatable cancer-targeted hydrogen peroxide probe for photoacoustic and fluorescence imaging. *Cancer Res.* **79**, 5407–5417 (2019).

18. S. Park, J. Kim, M. Jeon, J. Song, C. Kim, In vivo photoacoustic and fluorescence cystography using clinically relevant dual modal indocyanine green. *Sensors* **14**, 19660–19668 (2014).
19. U. Chitgupi, N. Nyayapathi, J. Kim, D. Wang, B. Sun, C. Li, K. Carter, W. C. Huang, C. Kim, J. Xia, Surfactant-stripped micelles for NIR-II photoacoustic imaging through 12 cm of breast tissue and whole human breasts. *Adv. Mater.* **31**, e1902279 (2019).
20. J. Levi, S.-R. Kothapalli, S. Bohndiek, J.-K. Yoon, A. Dragulescu-Andrasi, C. Nielsen, A. Tisma, S. Bodapati, G. Gowrishankar, X. Yan, Molecular photoacoustic imaging of follicular thyroid carcinoma. *Clin. Cancer Res.* **19**, 1494–1502 (2013).
21. Y. Cao, J. Hui, A. Kole, P. Wang, Q. Yu, W. Chen, M. Sturek, J.-X. Cheng, High-sensitivity intravascular photoacoustic imaging of lipid–laden plaque with a collinear catheter design. *Sci. Rep.* **6**, 25236 (2016).
22. J.-M. Yang, C. Favazza, R. Chen, J. Yao, X. Cai, K. Maslov, Q. Zhou, K. K. Shung, L. V. Wang, Simultaneous functional photoacoustic and ultrasonic endoscopy of internal organs in vivo. *Nat. Med.* **18**, 1297–1302 (2012).
23. A. Karlas, M. A. Pleitez, J. Aguirre, V. Ntziachristos, Optoacoustic imaging in endocrinology and metabolism. *Nat. Rev. Endocr.* **17**, 323–335 (2021).
24. M. Polkowski, C. Jenssen, P. Kaye, S. Carrara, P. Deprez, A. Gines, G. Fernández-Esparrach, P. Eisendrath, G. P. Aithal, P. Arcidiacono, Technical aspects of endoscopic ultrasound (EUS)-guided sampling in gastroenterology: European Society of Gastrointestinal Endoscopy (ESGE) technical guideline–March 2017. *Endoscopy* **49**, 989–1006 (2017).
25. M. S. Ali, W. Trick, B. I. Mba, D. Mohananey, J. Sethi, A. I. Musani, Radial endobronchial ultrasound for the diagnosis of peripheral pulmonary lesions: A systematic review and meta-analysis. *Respirology* **22**, 443–453 (2017).
26. J. Iglesias-Garcia, B. Lindkvist, J. Lariño-Noia, J. E. Domínguez-Muñoz, Endoscopic ultrasound elastography. *Endosc. Ultrasound* **1**, 8–16 (2012).
27. H. Guo, Y. Li, W. Qi, L. Xi, Photoacoustic endoscopy: A progress review. *J. Biophotonics* **13**, e202000217 (2020).
28. M. Basij, Y. Yan, S. S. Alshahrani, H. Helmi, T. K. Burton, J. W. Burmeister, M. M. Dominello, I. S. Winer, M. Mehrmohammadi, Miniaturized phased-array ultrasound and photoacoustic endoscopic imaging system. *Photoacoustics* **15**, 100139 (2019).
29. Y. Li, R. Lin, C. Liu, J. Chen, H. Liu, R. Zheng, X. Gong, L. Song, In vivo photoacoustic/ ultrasonic dual-modality endoscopy with a miniaturized full field-of-view catheter. *J. Biophotonics* **11**, e201800034 (2018).
30. L. Wang, P. Lei, X. Wen, P. Zhang, S. Yang, Tapered fiber-based intravascular photoacoustic endoscopy for high-resolution and deep-penetration imaging of lipid-rich plaque. *Opt. Express* **27**, 12832–12840 (2019).
31. Y. Li, Z. Zhu, J. C. Jing, J. J. Chen, A. E. Heidari, Y. He, J. Zhu, T. Ma, M. Yu, Q. Zhou, High-speed integrated endoscopic photoacoustic and ultrasound imaging system. *IEEE J. Sel. Top. Quantum Electron.* **25**, 7102005 (2018).
32. Y. Li, G. Lu, J. J. Chen, J. C. Jing, T. Huo, R. Chen, L. Jiang, Q. Zhou, Z. Chen, PMN-PT/Epoxy 1-3 composite based ultrasonic transducer for dual-modality photoacoustic and ultrasound endoscopy. *Photoacoustics* **15**, 100138 (2019).
33. P. Lei, X. Wen, L. Wang, P. Zhang, S. Yang, Ultrafine intravascular photoacoustic endoscope with a 0.7 mm diameter probe. *Opt. Lett.* **44**, 5406–5409 (2019).
34. Z. Xie, C. Shu, D. Yang, H. Chen, C. Chen, G. Dai, K. H. Lam, J. Zhang, X. Wang, Z. Sheng, In vivo intravascular photoacoustic imaging at a high speed of 100 frames per second. *Biomed. Opt. Express* **11**, 6721–6731 (2020).
35. W. Liu, Y. Zhou, M. Wang, L. Li, E. Vienneau, R. Chen, J. Luo, C. Xu, Q. Zhou, L. V. Wang, Correcting the limited view in optical-resolution photoacoustic microscopy. *J. Biophotonics* **11**, e201700196 (2018).
36. X. Bai, X. Gong, W. Hau, R. Lin, J. Zheng, C. Liu, C. Zeng, X. Zou, H. Zheng, L. Song, Intravascular optical-resolution photoacoustic tomography with a 1.1 mm diameter catheter. *PLOS ONE* **9**, e92463 (2014).
37. Z. Piao, T. Ma, J. Li, M. T. Wiedmann, S. Huang, M. Yu, K. Kirk Shung, Q. Zhou, C.-S. Kim, Z. Chen, High speed intravascular photoacoustic imaging with fast optical parametric oscillator laser at 1.7 μ m. *Appl. Phys. Lett.* **107**, 083701 (2015).
38. Y. Cao, M. Alloosh, M. Sturek, J. X. Cheng, Highly sensitive lipid detection and localization in atherosclerotic plaque with a dual-frequency intravascular photoacoustic/ultrasound catheter. *Transl. Biophotonics* **2**, e202000004 (2020).
39. H. Sun, W. Wang, Z. Zhang, L. Wang, W. Zhang, K. Xiong, S. Yang, Real-time optical-resolution photoacoustic endoscope. *Appl. Phys. Express* **14**, 042012 (2021).
40. Y. Qu, C. Li, J. Shi, R. Chen, S. Xu, H. Rafsanjani, K. Maslov, H. Krigman, L. Garvey, P. Hu, P. Zhao, K. Meyers, E. Diveley, S. Pizzella, L. Muench, N. Punyamurthy, N. Goldstein, O. Onwumere, M. Alisio, K. Meyenburg, J. Maynard, K. Helm, J. Slaughter, S. Barber, T. Burger, C. Kramer, J. Chubiz, M. Anderson, R. McCarthy, S. K. England, G. A. Macones, Q. Zhou, K. K. Shung, J. Zou, M. J. Stout, M. Tuuli, L. V. Wang, Transvaginal fast-scanning optical-resolution photoacoustic endoscopy. *J. Biomed. Opt.* **23**, 121617 (2018).
41. K. Xiong, S. Yang, X. Li, D. Xing, Autofocusing optical-resolution photoacoustic endoscopy. *Opt. Lett.* **43**, 1846–1849 (2018).
42. J.-M. Yang, K. Maslov, H.-C. Yang, Q. Zhou, K. K. Shung, L. V. Wang, Photoacoustic endoscopy. *Opt. Lett.* **34**, 1591–1593 (2009).
43. H. He, A. Stylogiannis, P. Afshari, T. Wiedemann, K. Steiger, A. Buehler, C. Zakian, V. Ntziachristos, Capsule optoacoustic endoscopy for esophageal imaging. *J. Biophotonics* **12**, e201800439 (2019).
44. R. Cao, J. Zhao, L. Li, L. Du, Y. Zhang, Y. Luo, L. Jiang, S. Davis, Q. Zhou, A. de la Zerda, Optical-resolution photoacoustic microscopy with a needle-shaped beam. *Nat. Photonics* **17**, 89–95 (2023).
45. H.-C. Hsu, L. Li, J. Yao, T. T. Wong, J. Shi, R. Chen, Q. Zhou, L. V. Wang, Dual-axis illumination for virtually augmenting the detection view of optical-resolution photoacoustic microscopy. *J. Biomed. Opt.* **23**, 076001 (2018).
46. B. Rao, R. Zhang, L. Li, J.-Y. Shao, L. V. Wang, Photoacoustic imaging of voltage responses beyond the optical diffusion limit. *Sci. Rep.* **7**, 2560 (2017).
47. L. Li, C. Yeh, S. Hu, L. Wang, B. T. Soetikno, R. Chen, Q. Zhou, K. Kirk Shung, K. I. Maslov, L. V. Wang, Fully motorized optical-resolution photoacoustic microscopy. *Opt. Lett.* **39**, 2117–2120 (2014).
48. L. Zhu, L. Li, L. Gao, L. V. Wang, Multi-view optical resolution photoacoustic microscopy. *Optica* **1**, 217–222 (2014).
49. J. Hui, Y. Cao, Y. Zhang, A. Kole, P. Wang, G. Yu, G. Eakins, M. Sturek, W. Chen, J.-X. Cheng, Real-time intravascular photoacoustic-ultrasound imaging of lipid-laden plaque in human coronary artery at 16 frames per second. *Sci. Rep.* **7**, 1417 (2017).
50. L. Lin, P. Zhang, S. Xu, J. Shi, L. Li, J. Yao, L. Wang, J. Zou, L. V. Wang, Handheld optical-resolution photoacoustic microscopy. *J. Biomed. Opt.* **22**, 041002 (2017).
51. Y. He, L. Wang, J. Shi, J. Yao, L. Li, R. Zhang, C.-H. Huang, J. Zou, L. V. Wang, In vivo label-free photoacoustic flow cytography and on-the-spot laser killing of single circulating melanoma cells. *Sci. Rep.* **6**, 39616 (2016).
52. J. Yao, L. Wang, J.-M. Yang, K. I. Maslov, T. T. Wong, L. Li, C.-H. Huang, J. Zou, L. V. Wang, High-speed label-free functional photoacoustic microscopy of mouse brain in action. *Nat. Methods* **12**, 407–410 (2015).
53. Y. S. Zhang, J. Yao, C. Zhang, L. Li, L. V. Wang, Y. Xia, Optical-resolution photoacoustic microscopy for volumetric and spectral analysis of histological and immunochemical samples. *Angew. Chem. Int. Ed. Engl.* **126**, 8237–8241 (2014).
54. R. Lin, Q. Zhang, S. Lv, J. Zhang, X. Wang, D. Shi, X. Gong, K.-H. Lam, Miniature intravascular photoacoustic endoscopy with coaxial excitation and detection. *J. Biophotonics* **16**, e202200269 (2023).
55. M. Kim, K. W. Lee, K. Kim, O. Gulenko, C. Lee, B. Keum, H. J. Chun, H. S. Choi, C. U. Kim, J.-M. Yang, Intra-instrument channel workable, optical-resolution photoacoustic and ultrasonic mini-probe system for gastrointestinal endoscopy. *Photoacoustics* **26**, 100346 (2022).
56. J. Park, B. Park, T. Y. Kim, S. Jung, W. J. Choi, J. Ahn, D. H. Yoon, J. Kim, S. Jeon, D. Lee, Quadruple ultrasound, photoacoustic, optical coherence, and fluorescence fusion imaging with a transparent ultrasound transducer. *Proc. Natl. Acad. Sci. U.S.A.* **118**, e1920879118 (2021).
57. S. Cho, M. Kim, J. Ahn, Y. Kim, J. Lim, J. Park, H. H. Kim, W. J. Kim, C. Kim, An ultrasensitive and broadband transparent ultrasound transducer for ultrasound and photoacoustic imaging in-vivo. *Nat. Commun.* **15**, 1444 (2024).
58. R. Lin, S. Lv, W. Lou, X. Wang, Z. Xie, S. Zeng, R. Chen, W. Gao, T. Jiang, K.-W. E. Cheng, In-vivo assessment of a rat rectal tumor using optical-resolution photoacoustic endoscopy. *Biomed. Opt. Express* **15**, 2251–2261 (2024).
59. J. Kim, J. Ahn, G. Kang, J. H. Hwang, C. Kim, High-resolution photoacoustic/ultrasound imaging of the porcine stomach wall: An ex vivo feasibility study. *Biomed. Opt. Express* **12**, 6717–6729 (2021).
60. J. W. Cho, The role of endoscopic ultrasonography in T staging: Early gastric cancer and esophageal cancer. *Clin. Endosc.* **46**, 239–242 (2013).
61. S. Y. Kim, K.-N. Shim, J.-H. Lee, J. Y. Lim, T. O. Kim, A. R. Choe, C. H. Tae, H.-K. Jung, C. M. Moon, S.-E. Kim, Comparison of the diagnostic ability of endoscopic ultrasonography and abdominopelvic computed tomography in the diagnosis of gastric subepithelial tumors. *Clin. Endosc.* **52**, 565–573 (2019).
62. J. Xiao, J. Jiang, J. Zhang, Y. Wang, B. Wang, Acoustic-resolution-based spectroscopic photoacoustic endoscopy towards molecular imaging in deep tissues. *Opt. Express* **30**, 35014–35028 (2022).
63. X. Li, K. Xiong, S. Yang, Large-depth-of-field optical-resolution colorectal photoacoustic endoscope. *Appl. Phys. Lett.* **114**, (2019).
64. H. He, L. Englert, V. Ntziachristos, Optoacoustic endoscopy of the gastrointestinal tract. *ACS Photonics* **10**, 559–570 (2023).
65. C. Qiu, B. Wang, N. Zhang, S. Zhang, J. Liu, D. Walker, Y. Wang, H. Tian, T. R. Shrout, Z. Xu, Transparent ferroelectric crystals with ultrahigh piezoelectricity. *Nature* **577**, 350–354 (2020).
66. M. Otoničar, A. Bradeško, S. Salmanov, C. Chung, J. Jones, T. Rojac, Effects of poling on the electrical and electromechanical response of PMN–PT relaxor ferroelectric ceramics. *Open Ceram.* **7**, 100140 (2021).
67. A. Kumar, W. Kim, P. Sriboriboon, H.-Y. Lee, Y. Kim, J. Ryu, AC poling-induced giant piezoelectricity and high mechanical quality factor in [001] PMN-PZT hard single crystals. *Sens. Actuators A Phys.* **372**, 115342 (2024).

68. V. I. Peinado, S. Pizarro, J. A. Barbera, Pulmonary vascular involvement in COPD. *Chest* **134**, 808–814 (2008).
69. S. M. Donat, Evaluation and follow-up strategies for superficial bladder cancer. *Urol. Clin. North Am.* **30**, 765–776 (2003).
70. T. Ma, "Multi-Modality Intravascular Imaging by Combined Use of Ultrasonic and Opticial Techniques", thesis, University of Southern California (2015).
71. X. Zhu, Q. Huang, A. DiSpirito, T. Vu, Q. Rong, X. Peng, H. Sheng, X. Shen, Q. Zhou, L. Jiang, Real-time whole-brain imaging of hemodynamics and oxygenation at micro-vessel resolution with ultrafast wide-field photoacoustic microscopy. *Light Sci. Appl.* **11**, 138 (2022).
72. L. Menozzi, Á. Del Águila, T. Vu, C. Ma, W. Yang, J. Yao, Three-dimensional non-invasive brain imaging of ischemic stroke by integrated photoacoustic, ultrasound and angiographic tomography (PAUSAT). *Photoacoustics* **29**, 100444 (2023).
73. J. Yao, A. A. Kaberniuk, L. Li, D. M. Shcherbakova, R. Zhang, L. Wang, G. Li, V. V. Verkhusha, L. V. Wang, Multiscale photoacoustic tomography using reversibly switchable bacterial phytochrome as a near-infrared photochromic probe. *Nat. Methods* **13**, 67–73 (2016).
74. L. Li, H. C. Hsu, V. V. Verkhusha, L. V. Wang, D. M. Shcherbakova, Multiscale photoacoustic tomography of a genetically encoded near-infrared FRET biosensor. *Adv. Sci.* **8**, e2102474 (2021).
75. L. Li, L. Zhu, C. Ma, L. Lin, J. Yao, L. Wang, K. Maslov, R. Zhang, W. Chen, J. Shi, Single-impulse panoramic photoacoustic computed tomography of small-animal whole-body dynamics at high spatiotemporal resolution. *Nat. Biomed. Eng.* **1**, 0071 (2017).
76. R. Krimholtz, D. A. Leedom, G. L. Matthaei, New equivalent circuits for elementary piezoelectric transducers. *Electron. Lett.* **6**, 398–399 (1970).

Acknowledgments

Funding: This research was supported by the Basic Science Research Program through the National Research Foundation of Korea (NRF) funded by the Ministry of Education (2020R1A6A1A03047902), by the National R&D Program through the National Research Foundation of Korea (NRF) funded by Ministry of Science and ICT (2021M3C1C3097624), by the Korea Medical Device Development Fund grant funded by the Korea government (the Ministry of Science and ICT, the Ministry of Trade, Industry and Energy, the Ministry of Health & Welfare, the Ministry of Food and Drug Safety) (project number: 1711195277, RS-2020-KD000008), and by BK21 FOUR project. This work was supported by the National Research Foundation of Korea (NRF) grant funded by the Korea government (MSIT) (NRF-2023R1A2C3004880). This work was supported by the National Research Foundation of Korea (NRF) grant funded by the Korea government (MSIT) (no. RS-2023-00212322). This study was supported by a grant from the Korean Gastrointestinal Endoscopy Research Foundation (2023 Investigation Grant). This research was supported by the Commercialization Promotion Agency for R&D Outcomes (COMPA) funded by the Ministry of Science and ICT (MSIT) (2710006567). This research was supported by the Ministry of Trade, Industry and Energy of the Republic of Korea (20024916). **Author contributions:** Conceptualization: C.K. and J.K. Methodology: J.K., D.H., S.C., J.P., J.A., M.K., D.K., and D.H.J. Investigation: J.K., D.H., M.H., and H.M.K. Visualization: J.K., S.C., and D.H. Supervision: C.K., H.M.K., and H.H.K. Writing–original draft: J.K., D.H., and C.K. Writing–review and editing: J.K., D.H., and C.K. **Competing interests:** C.K., J.K., S.C., and J.A. have financial interests in OPTICHO, which did not support this work. J.K., D.H., S.C., J.P., H.H.K., and C.K. are authors on a pending patent related to this work filed by POSTECH Research and Development Foundation (no. KR20220141507A, filed 13 April 2021). The other authors declare that they have no competing interests. **Data and materials availability:** All data needed to evaluate the conclusions in the paper are present in the paper and/or the Supplementary Materials.

Submitted 12 June 2024
Accepted 22 October 2024
Published 22 November 2024
10.1126/sciadv.adq9960